

From viral evolution to spatial contagion: a biologically modulated Hawkes model

Andrew J. Holbrook¹, Xiang Ji² and Marc A. Suchard^{1,3,4}

¹Department of Biostatistics, University of California, Los Angeles

²Department of Mathematics, Tulane University

³Department of Biomathematics, University of California, Los Angeles

⁴Department of Human Genetics, University of California, Los Angeles

Abstract

Mutations sometimes increase contagiousness for evolving pathogens. During an epidemic, scientists use viral genome data to infer a shared evolutionary history and connect this history to geographic spread. We propose a model that directly relates a pathogen’s evolution to its spatial contagion dynamics—effectively combining the two epidemiological paradigms of phylogenetic inference and self-exciting process modeling—and apply this *phylogenetic Hawkes process* to a Bayesian analysis of 23,422 viral cases from the 2014-2016 Ebola outbreak in West Africa. The proposed model is able to detect individual viruses with significantly elevated rates of spatiotemporal propagation for a subset of 1,610 samples that provide genome data. Finally, to facilitate model application in big data settings, we develop massively parallel implementations for the gradient and Hessian of the log-likelihood and apply our high performance computing framework within an adaptively preconditioned Hamiltonian Monte Carlo routine.

Keywords Bayesian phylogeography; Ebola virus; parallel computing; spatiotemporal Hawkes processes.

1 Introduction

The COVID-19 pandemic has demonstrated the need for new scientific tools for the analysis and prediction of viral contagion across human landscapes. The mathematical characterization of the complex relationships underlying pathogen genetics and spatial contagion stands as a central challenge of 21st century epidemiology. We approach this task by unifying two distinct probabilistic approaches to viral modeling. On the one hand, Bayesian phylogenetics (Sinsheimer et al., 1996; Yang and Rannala, 1997; Mau et al., 1999; Suchard et al., 2001) uses genetic sequences from a limited collection of viral samples to integrate over high-probability shared evolutionary histories in the form of *phylogenies* or family trees. On the other hand,

| | Traditional Bayesian phylogenetics | Hawkes processes |
|-----------------------|------------------------------------|-------------------------------|
| Observational limit | N in low thousands | N in high tens-of-thousands |
| Biological insight | Evolutionary history | None |
| Genetic sequencing | Required | Not required |
| Spatiotemporal data | Not required | Required |
| Geographic spread | Not modeled | Modeled |
| Large-scale transport | Does not induce bias | Induces bias |

Table 1: Comparison of two probabilistic modeling paradigms within viral epidemiology, the combination of which represents a new tool for Bayesian phylogeography.

self-exciting, spatiotemporal Hawkes processes (Reinhart, 2018) model spatial contagion by allowing an observed event to increase the probability of additional observations nearby and in the immediate future.

Both modeling paradigms come with their own advantages. For Bayesian phylogenetics, the past twenty years have witnessed a slew of high-impact scientific studies in viral epidemiology (Rambaut et al., 2008; Smith et al., 2009; Faria et al., 2014; Gire et al., 2014; Dudas et al., 2017; Boni et al., 2020) and the rise of powerful computing tools facilitating inference from expressive, hierarchical models of phylogenies and evolving traits (Ronquist et al., 2012; Suchard et al., 2018). Unfortunately, the number of evolutionary trees to integrate over explodes with the number of viral samples analyzed (Felsenstein, 1978), so Bayesian phylogenetic analyses typically restrict to a relatively small number of viral samples, at most totaling a few thousand. The fact that viral cases that undergo genetic sequencing usually represent a small subset of the total case count exacerbates this issue. Thus, failure to detect phylogenetic clades that represent novel strains on account of computational and surveillance limitations always remains a possibility. Until now, these weaknesses have also held for the sub-discipline of Bayesian phylogeography, which attempts to relate viral evolutionary histories to geographic spread as represented by (typically Brownian) phylogenetic diffusions. These models describe viral spread through either discretized (Lemey et al., 2009) or continuous (Lemey et al., 2010) space, but both approaches induce their own form of bias (Holbrook et al., 2020). In the face of these shortcomings, Bayesian phylogeography needs new tools for directly modeling spatial contagion.

Hawkes processes (Hawkes, 1971a,b, 1972, 1973, 2018) are widely applicable point process models for generally viral or contagious phenomena, such as earthquakes and aftershocks (Hawkes, 1973; Ogata, 1988; Zhuang et al., 2004; Fox et al., 2016), financial stock trading (Bacry et al., 2015; Hawkes, 2018), viral content on social media (Rizoiu et al., 2017; Kobayashi and Lambiotte, 2016), gang violence (Mohler et al., 2013; Mohler, 2014; Loeffler and Flaxman, 2018; Park et al., 2019; Holbrook et al., 2021) and wildfires (Schoenberg, 2004). Unsurprisingly, Hawkes processes are natural models for the contagion dynamics of biological viruses as well. Kim (2011) uses spatiotemporal Hawkes processes (Reinhart, 2018), which model viral cases as unmarked events in space and time, to model the spread of avian influenza virus (H5N1). Meyer et al. (2014) incorporate power laws to describe spatial contagion dynamics and model meningococcal disease in Germany from 2001 to 2008. While Rizoiu et al. (2018) do not model epidemiological data, they do draw connections between

epidemiological SIR models and Hawkes processes, showing that the rate of events in the SIR model is equal to that of a finite-population Hawkes model. Kelly et al. (2019) apply a temporal nonparametric Hawkes process to the 2018-2019 Ebola outbreak in the Democratic Republic of the Congo and successfully generate accurate disease prevalence forecasts. Chiang et al. (2020) model COVID-19 cases and deaths in the U.S. at the county level using spatially indexed mobility and population data to modify the process conditional intensity. Most recently, Bertozzi et al. (2020) compare the performance of a temporal Hawkes process model with temporally evolving conditional intensity to that of SIR and SEIR models for modeling regional COVID-19 case dynamics.

Because such Hawkes processes do not involve genetic information, one may apply the model to a much larger collection of cases, i.e., those for which a timestamp and spatial coordinates are available. Moreover, recent successes in scaling Hawkes process inference to a big data setting enable inference from observations numbered in the high tens-of-thousands (Holbrook et al., 2021; Yuan et al., 2021). This ability to interface with an order of magnitude more cases represents a major benefit of the Hawkes process in comparison to the Bayesian phylogenetic paradigm, but the trade-off is that conclusions drawn from a Hawkes process analysis are devoid of explicit biological insight. It is possible for the model to attribute self-exciting dynamics to nearby viral cases that are only distantly related on the phylogenetic tree. Finally, these processes do not immediately account for viral spread through large-scale transportation networks (Brockmann and Helbing, 2013; Holbrook et al., 2020) but attribute events resulting from such contagion to a ‘background’ process.

In the following, we construct a Bayesian hierarchical model that allows both modeling approaches to support each other. This model (Figure 1) learns phylogenetic trees that describe the evolutionary history of the subset of observations that yield genetic sequencing and uses this history to inform the distribution of a latent relative rate or *productivity* (Schoenberg et al., 2019; Schoenberg, 2020) for each virus in this limited set. In turn, these virus-specific rates modify the rate of self-excitation of a spatiotemporal Hawkes process describing the contagion of all viruses, sequenced or not. We use a Metropolis-within-Gibbs strategy to jointly infer all parameters and latent variables of our phylogenetic Hawkes process and overcome the $O(N^2)$ computational complexity of the Hawkes process likelihood by incorporating the modified likelihood in the HPHAWKES open-source, high-performance computing library (Holbrook et al., 2021) available at <https://github.com/suchard-group/hawkes>. Within the same library, we also develop multiple parallel computing algorithms for the log-likelihood gradient and Hessian with respect to the model’s virus-specific rates. GPU-based implementations of these gradient and Hessian calculations score hundred-fold speedups over single-core computing and help overcome quadratic complexity in the context of an adaptively preconditioned Hamiltonian Monte Carlo (Neal, 2011). These speedups prove useful in our analysis of 23,422 viral cases from the 2014-2016 Ebola outbreak in West Africa.

2 Methods

We develop the phylogenetic Hawkes process and its efficient inference in the following sections. Importantly, our proposed hierarchical model integrates both sequenced and unsequenced viral case data, representing a significant and clear contribution insofar as:

1. the percentage of confirmed viral cases sequenced during an epidemic is often in the single digits (Wadman, 2021);
2. and previous phylogeographic models have failed to leverage additional information provided by geolocated, unsequenced case data.

We address this shortcoming by constructing a new hierarchical model that *both* models all spatiotemporal data with a Hawkes process (Section 2.1) *and* allows an inferred evolutionary history in the form of a phylogenetic tree to influence dependencies between relative rates of contagion (Section 2.2) for the small subset of viral cases for which genome data are available. We believe that this approach is altogether novel.

2.1 Spatiotemporal Hawkes process for viral contagion

Hawkes processes (Hawkes, 1971a,b, 1972, 2018) constitute a useful class of inhomogeneous Poisson point processes (Daley and Jones, 2003) for which individual events contribute to an increased rate of future events. Spatiotemporal Hawkes processes (Reinhart, 2018) are marked Hawkes processes with spatial coordinates for marks (Daley and Jones, 2003). We are interested in spatiotemporal Hawkes processes with infinitesimal rate

$$\lambda(\mathbf{x}, t) = \mu(\mathbf{x}) + \xi(\mathbf{x}, t) = \mu(\mathbf{x}) + \sum_{t_n < t} g_n(\mathbf{x} - \mathbf{x}_n, t - t_n),$$

where $\mathbf{x} \in \mathbb{R}^D$, $t \in \mathbb{R}^+$ and the subscript n indicates that the usual triggering function $g(\cdot, \cdot)$ takes on different forms depending on some characteristic associated with event n . These non-negative, monotonically non-increasing, event-indexed triggering functions additively contribute to $\xi(\cdot, \cdot)$, the *self-excitatory* rate component, and encourage this rate to increase after each observed event. Here, $\mu(\cdot)$ is the *background* rate and only depends on spatial position \mathbf{x} . Conditioned on observations (\mathbf{x}_n, t_n) , $n = 1, \dots, N$, we specify the rate components

$$\mu(\mathbf{x}) = \frac{\mu_0}{\tau_x^D} \sum_{n=1}^N \phi\left(\frac{\mathbf{x} - \mathbf{x}_n}{\tau_x}\right) \mathcal{I}_{[x \neq x_n]} \quad \text{and} \quad \xi(\mathbf{x}, t) = \frac{\theta_0 \omega}{h^D} \sum_{t_n < t} \theta_n e^{-\omega(t-t_n)} \phi\left(\frac{\mathbf{x} - \mathbf{x}_n}{h}\right),$$

where $\tau_x > 0$ and $h > 0$ are the background and self-excitatory spatial lengthscales, $\mu_0 > 0$ and $\theta_0 > 0$ are the background and self-excitatory weights, $1/\omega > 0$ is the self-excitatory temporal lengthscale, $\phi(\cdot)$ is the D -dimensional standard normal probability density function, and the background rate's indicator function prevents a trivial maximum at $\tau_x \rightarrow 0$ (Habbema et al., 1974; Robert, 1976). The inclusion of $\theta_n > 0$ for $n = 1, \dots, N$ within the self-excitatory rate marks a major departure from similar model specifications in Loeffler and Flaxman (2018); Holbrook et al. (2021). These ‘degrees of contagion’ or ‘productivities’ (Schoenberg et al., 2019; Schoenberg, 2020) allow different events to contribute differently to the overall self-excitatory rate of the process: the larger the θ_n , the higher the rate directly following event n (Figure 1, right). Following the connection of the Hawkes process with exponential triggering function to a discrete time SIR model (Rizoiu et al., 2018), Bertozzi et al. (2020) refer to these quantities as a reproduction number. In the following, we refer

to θ_n as the *event-specific*, *case-specific* or *virus-specific* rate for the n th event, case or viral observation.

Denoting $\boldsymbol{\theta} = (\theta_1, \dots, \theta_N)^T$, the likelihood of observing data $(\mathbf{X}, \mathbf{t}) = ((\mathbf{x}_1, t_1), \dots, (\mathbf{x}_N, t_N))^T$ is (Daley and Jones, 2003)

$$\mathcal{L}(\mathbf{X}, \mathbf{t} | \mu_0, \tau_x, \theta_0, \boldsymbol{\theta}, \omega, h) = \exp \left(- \int_{\mathbb{R}^D} \int_0^{t_N} \lambda(\mathbf{x}, t) dt d\mathbf{x} \right) \prod_{n=1}^N \lambda(\mathbf{x}_n, t_n) := e^{-\Lambda(t_N)} \cdot \prod_{n=1}^N \lambda_n.$$

The choice of \mathbb{R}^D for integration domain is popular and often necessary but assumes complete observation over the entirety of \mathbb{R}^D (Schoenberg, 2013). The resulting integral may be written (Appendix A)

$$\Lambda(t_N) = \mu_0 t_N - \theta_0 \sum_{n=1}^N \theta_n (e^{-\omega(t_N - t_n)} - 1) := \sum_{n=1}^N \Lambda_n,$$

leading to a log-likelihood of

$$\begin{aligned} \ell(\mathbf{X}, \mathbf{t} | \mu_0, \tau_x, \theta_0, \boldsymbol{\theta}, \omega, h) &= -\Lambda(t_N) + \sum_{n=1}^N \log \lambda_n \tag{1} \\ &= \sum_{n=1}^N \left\{ \log \left[\sum_{n'=1}^N \left(\frac{\mu_0 \mathcal{I}_{[\mathbf{x}_n \neq \mathbf{x}_{n'}]}}{\tau_x^D} \phi \left(\frac{\mathbf{x}_n - \mathbf{x}_{n'}}{\tau_x} \right) \right. \right. \right. \\ &\quad \left. \left. \left. + \frac{\theta_0 \theta_{n'} \omega \mathcal{I}_{[t_{n'} < t_n]}}{h^D} e^{-\omega(t_n - t_{n'})} \phi \left(\frac{\mathbf{x}_n - \mathbf{x}_{n'}}{h} \right) \right) \right] - \Lambda_n \right\} \\ &:= \sum_{n=1}^N \left[\log \left(\sum_{n'=1}^N \lambda_{nn'} \right) - \Lambda_n \right] := \sum_{n=1}^N \ell_n. \end{aligned}$$

We reference these formulas while outlining our inference strategy in Section 2.3 and detailing our massively parallel algorithms for calculating the log-likelihood gradient and Hessian with respect to event-specific rates $\boldsymbol{\theta}$ in Appendix C. We describe our biologically modulated joint prior on event-specific rates $\theta_1, \dots, \theta_N$ in the next section.

2.2 Phylogenetic Brownian process prior on rates

We use standard Bayesian phylogenetics hierarchical approaches (Suchard et al., 2003) to model a single molecular sequence alignment \mathbf{S} containing sequences from $M \leq N$ evolutionarily related viruses. Let \mathcal{M} denote the ordered index set with cardinality $|\mathcal{M}| = M$ containing every number within the set $\{1, \dots, N\}$ that corresponds to an observed virus for which genome data are present. In the following, we number the elements within \mathcal{M} as m_1, m_2, \dots, m_M . Moreover, we make use of the set \mathcal{M}^+ with cardinality $|\mathcal{M}^+| = 2M - 1$, satisfying $\mathcal{M} \subset \mathcal{M}^+$ and containing elements m_1, \dots, m_{2M-1} . Our primary object of interest is the phylogenetic tree \mathcal{G} (Figure 1, left) defined as a bifurcating, directed graph with M terminal degree-1 nodes $(\nu_{m_1}, \dots, \nu_{m_M})$ that correspond to the tips of the tree (or

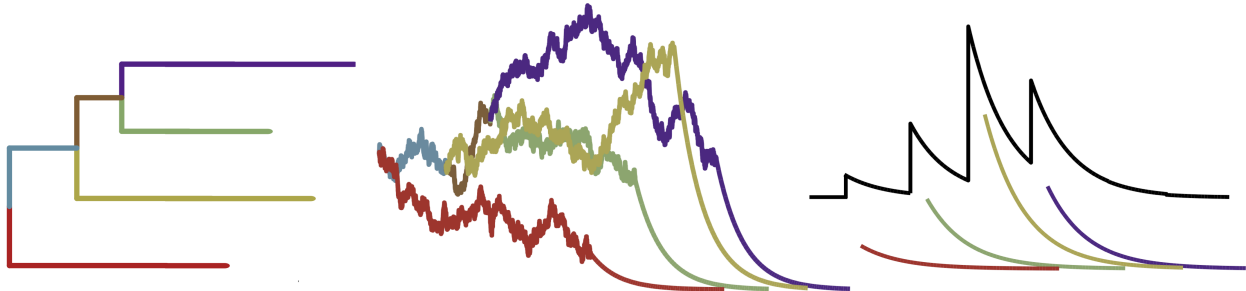


Figure 1: The phylogenetic Hawkes process relates the evolutionary history of a virus to the rate at which subsequent viral cases occur nearby. Left: a phylogenetic tree characterizes the evolution of a viral strain. Middle: a Brownian motion ‘along the tree’ describes the evolution of infinitesimal rates as a function of branch lengths and tree topology (Section 2.2). Right: virus-specific rates additively contribute to the rate of occurrence for future cases (Section 2.1).

sequenced observations), $M - 2$ internal degree-3 nodes $(\nu_{m_{M+1}}, \dots, \nu_{m_{2M-2}})$, a root degree-2 node $\nu_{m_{2M-1}}$ and edge weights $(w_{m_1}, \dots, w_{m_{2M-2}})$ that encode the elapsed evolutionary time between nodes. Here, each w_m communicates the expected number of molecular substitutions per site, which is itself the product between the real time duration and the evolutionary rate arising from a molecular clock model. For example, we use a relaxed molecular clock model (Drummond et al., 2006b) that allows for substitution rates to flexibly vary across branches (Section 3.2). One may either know \mathcal{G} *a priori* or endow it with a prior distribution parameterized by some vector ϕ . Suchard et al. (2001) and Suchard et al. (2018) develop the joint distribution $p(\mathbf{S}, \phi, \mathcal{G})$ in detail.

We assume that the event-specific rates θ defined within our Hawkes model take the form (Figure 1, middle)

$$\begin{cases} \theta_n = \theta_n(z_n) = \exp(z_n + \beta^T \mathbf{f}(t_n)) & z_n \in \mathbb{R}, \quad n \in \mathcal{M} \\ \theta_n = 1 & n \notin \mathcal{M}, \end{cases}$$

and that the elements of vector $\mathbf{z} = (z_{m_1}, \dots, z_{m_M})^T$ follow a Brownian diffusion process along the branches of \mathcal{G} (Cavalli-Sforza and Edwards, 1967; Felsenstein, 1985; Lemey et al., 2010). Here, $\mathbf{f}(\cdot)$ is some fixed vector function and the inclusion of the linear term $\beta^T \mathbf{f}(t_n)$ helps control for global trends resulting from extrinsic events such as mass quarantine or travel restrictions. Under the Brownian process, the latent value of a child node ν_c in tree \mathcal{G} is normally distributed about the value of its parent node $\nu_{\text{pa}(c)}$ with variance $w_c \times \sigma^2$, where σ^2 gives the dispersal rate after controlling for correlation in values that are shared by descent through the phylogenetic tree \mathcal{G} . We further posit that the latent value of the root node $\nu_{m_{2M-1}}$ is *a priori* normally distributed with mean 0 and variance $\tau_0 \times \sigma^2$. The vector \mathbf{z} is then multivariate normally distributed Cybis et al. (2015) and has probability density function

$$p(\mathbf{z} | \mathbf{V}_G, \sigma^2, \tau_0) = (2\pi\sigma^2)^{-M/2} |\mathbf{V}_G|^{-1/2} \exp\left(-\frac{1}{2\sigma^2} \mathbf{z}^T \mathbf{V}_G^{-1} \mathbf{z}\right), \quad (2)$$

where $\mathbf{V}_{\mathcal{G}} = \{v_{nm}\}$ is a symmetric, positive definite, block-diagonal $M \times M$ matrix with structure dictated by \mathcal{G} . Defining $d_F(u, v)$ to be the sum of edge-weights along the shortest path between nodes u and v in tree \mathcal{G} , the diagonal elements $v_{mm} = \tau_0 + d_F(\nu_{m_{2M-1}}, \nu_{m_m})$ are the elapsed evolutionary time between the root node and tip node m_m , and off-diagonal elements $v_{nm} = \tau_0 + [d_F(\nu_{m_{2M-1}}, \nu_{m_n}) + d_F(\nu_{m_{2M-1}}, \nu_{m_m}) - d_F(\nu_{m_n}, \nu_{m_m})] / 2$ are the evolutionary time period between the root node and the most recent common ancestor of tip nodes m_n and m_m .

2.3 Inference

Due to the complexity of the phylogenetic Hawkes process and the large number of viruses we seek to model, we must use advanced statistical, algorithmic and computational tools to infer the posterior distribution

$$p(\sigma^2, \mathcal{G}, \phi, \mu_0, \tau_x, \theta_0, \theta, \omega, h, \beta | \mathbf{X}, \mathbf{t}, \mathbf{S}) \propto \mathcal{L}(\mathbf{X}, \mathbf{t} | \mu_0, \tau_x, \theta_0, \theta(\mathbf{z}), \omega, h) \times p(\mathbf{z} | \sigma^2, \mathcal{G}) \times \quad (3)$$

$$p(\mu_0) \times p(\tau_x) \times p(\theta_0) \times p(\omega) \times p(h) \times p(\beta) \times$$

$$p(\sigma^2) \times p(\mathbf{S}, \phi, \mathcal{G}).$$

We do so using a random-scan Metropolis-with-Gibbs scheme, in which we compute key quantities with the help of adaptively preconditioned Hamiltonian Monte Carlo (HMC) (Neal, 2011), dynamic programming and parallel computing on cutting-edge graphics processing units (GPU).

2.3.1 Dynamic programming for phylogenetic diffusion quantities

We must evaluate $p(\mathbf{z} | \sigma^2, \mathcal{G})$ to sample \mathcal{G} . The bottleneck within the evaluation of Equation (2) is the ostensibly $\mathcal{O}(M^3)$ matrix inverse $\mathbf{V}_{\mathcal{G}}^{-1}$, but Pybus et al. (2012) develop a dynamic programming algorithm to perform the requisite computations in $\mathcal{O}(M)$ with parallelized post-order traversals of \mathcal{G} . We use this algorithm, which is closely related to the linear-time algorithms of Freckleton (2012) and Ho and Ané (2014), as all are examples of message passing on a directed, acyclic graph (Cavalli-Sforza and Edwards, 1967; Pearl, 1982). Similar tricks render inference for ϕ linear in M , and Fisher et al. (2021) extend Pybus et al. (2012) to compute gradients with respect to ϕ . Finally, implementing these algorithms on GPUs would lead to additional speedups (Suchard and Rambaut, 2009), but the computational bottleneck we face when applying the phylogenetic Hawkes process arises from the Hawkes process likelihood and its gradients.

2.3.2 Massive parallelization for Hawkes model quantities

Sampling the Hawkes process parameters $\mu_0, \tau_x, \theta_0, \omega, h, \beta$ and event-specific rates θ requires evaluation of the likelihood $\mathcal{L}(\mathbf{X}, \mathbf{t} | \mu_0, \tau_x, \theta_0, \theta, \omega, h)$ or its logarithm. Unfortunately, the double summation of Equation (1) results in an $\mathcal{O}(N^2)$ computational complexity that makes repeated likelihood evaluations all but impossible for the number of observations considered in this paper. We therefore use the high-performance computing framework of Holbrook et al. (2021) to massively parallelize likelihood evaluations in the context of univariate, adaptive Metropolis-Hastings proposals for parameters $\mu_0, \tau_x, \theta_0, \omega, h$ and β . On the other

hand, inference for the M -vector \mathbf{z} requires more than fast univariate proposals, so we opt for HMC to sample from its high-dimensional posterior. Even in high dimensions, HMC efficiently generates proposal states by simulating a physical Hamiltonian system that renders the target posterior distribution invariant. Here, we follow standard procedure and specify the system with total energy

$$H(\mathbf{z}, \mathbf{p}) = -\log(\pi(\mathbf{z}) \xi(\mathbf{p}|\mathbf{M})) \propto -\log \pi(\mathbf{z}) + \frac{1}{2} \mathbf{p}^T \mathbf{M}^{-1} \mathbf{p},$$

where $\pi(\mathbf{z})$ is the density of the marginal posterior for \mathbf{z} , \mathbf{p} is a Gaussian distributed ‘momentum’ variable with density $\xi(\mathbf{p}|\mathbf{M})$, and \mathbf{M} is the system mass matrix and the covariance of \mathbf{p} . We again follow standard HMC procedure and use the leapfrog algorithm (Leimkuhler and Reich, 2004) to integrate Hamilton’s equations

$$\dot{\mathbf{z}} = \frac{\partial}{\partial \mathbf{p}} H(\mathbf{z}, \mathbf{p}) = \frac{1}{2} \mathbf{M}^{-1} \mathbf{p}, \quad \dot{\mathbf{p}} = -\frac{\partial}{\partial \mathbf{z}} H(\mathbf{z}, \mathbf{p}) = \nabla \log \pi(\mathbf{z}).$$

But there is no free lunch: simulation of the physical system requires repeated evaluations of the log-likelihood gradient, and these evaluations may become burdensome in big data contexts. Indeed, the gradient of the Hawkes process log-likelihood of Equation (1) with respect to $\boldsymbol{\theta}$ becomes computationally onerous for large N and M . The gradient with respect to a single event-specific rate θ_m takes the form

$$\begin{aligned} \frac{\partial \ell}{\partial \theta_m} &= -\frac{\partial \Lambda_m}{\partial \theta_m} + \sum_{t_m < t_n} \frac{1}{\lambda_n} \frac{\partial \lambda_{nm}}{\partial \theta_m} \\ &= \theta_0 (e^{-\omega(t_N - t_m)} - 1) + \sum_{t_m < t_n} \frac{1}{\lambda_n} \frac{\theta_0 \omega}{h^D} e^{-\omega(t_n - t_m)} \phi \left(\frac{\mathbf{x}_n - \mathbf{x}_m}{h} \right), \end{aligned} \quad (4)$$

where the summation and λ_n are both of complexity $\mathcal{O}(N)$. Thus, computing the entire vector $\partial \ell / \partial \boldsymbol{\theta} = (\partial \ell / \partial \theta_1, \dots, \partial \ell / \partial \theta_M)^T$ requires time $\mathcal{O}(NM)$. Worse still, due to the multiscale nature of the posterior for the relative rates (Figure 4), we find it necessary to precondition the Hamiltonian dynamics by specifying a diagonal mass matrix with elements

$$\mathbf{M}_{mm}^{-1} \approx -\frac{\partial^2 \ell}{\partial \theta_m^2} = \sum_{t_m < t_n} \frac{1}{\lambda_n^2} \frac{\theta_0^2 \omega^2}{h^{2D}} e^{-2\omega(t_n - t_m)} \phi^2 \left(\frac{\mathbf{x}_n - \mathbf{x}_m}{h} \right). \quad (5)$$

Specifically, we maintain a running average of Hessians calculated at a fixed interval and use this as our preconditioner \mathbf{M} , thus maintaining asymptotic unbiasedness of Monte Carlo estimates (Haario et al., 2001). Just as with the gradient, the summation and λ_n are both of complexity $\mathcal{O}(N)$, and the resulting complexity for the entire Hessian is $\mathcal{O}(NM)$. To overcome these rate-limiting steps, we develop massively parallel central processing unit (CPU) and GPU implementations of both the gradient and the Hessian. Although our GPU-based implementations are fastest (Section 3.1), our CPU implementations are competitive, making use of both multi-core processing and SIMD (single instruction, multiple data) vectorization (Holbrook et al., 2020). Regardless of implementation, all of our high-performance software remains freely available for public use.

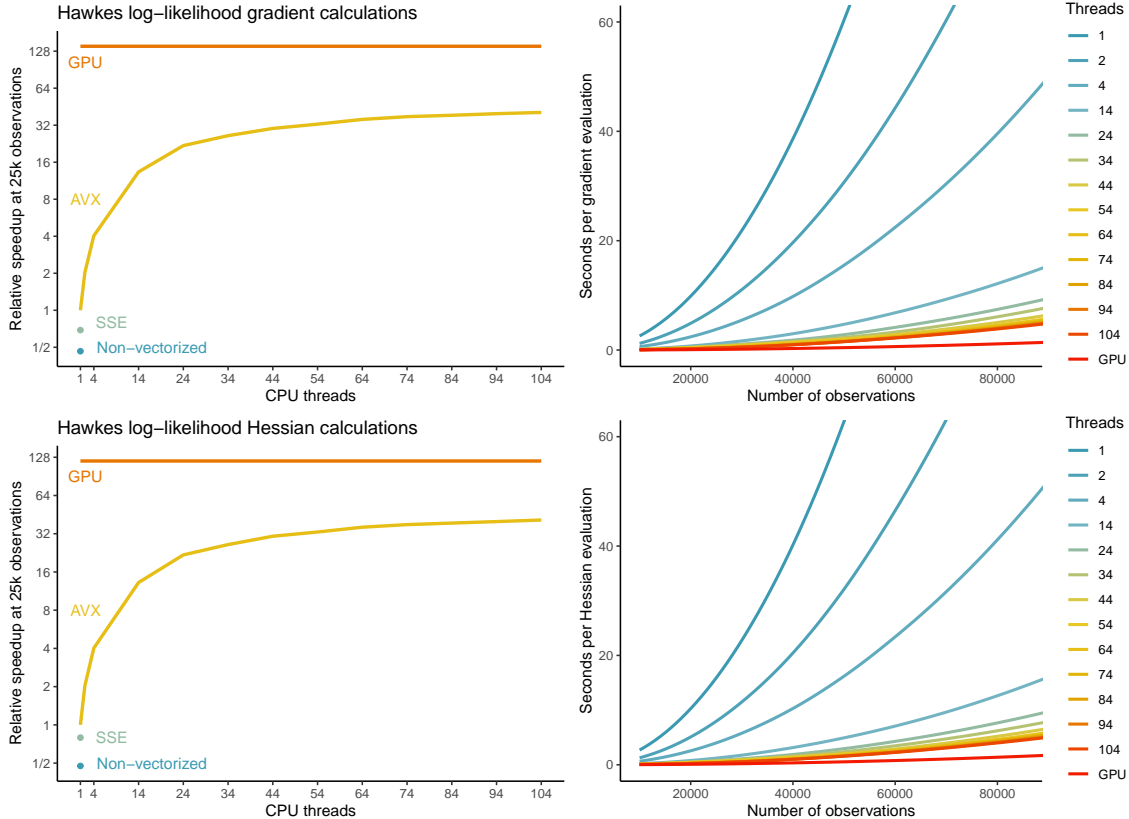


Figure 2: Spatiotemporal Hawkes process log-likelihood gradient and Hessian calculations with respect to event-specific rates θ with central and graphics processing units (CPU and GPU). [Left] Multiplicative speedups over single-threaded advanced vector extensions (AVX) vectorization for single-threaded non-vectorized and streaming SIMD extensions (SSE), multi-threaded AVX and many-core GPU processing for 25,000 randomly generated data points. [Right] Seconds per gradient and Hessian calculations for multi-threaded AVX and GPU implementations from 10 to 90 thousand data points.

2.4 Software availability

We use the Bayesian evolutionary analysis by sampling trees (BEAST) software package (Suchard et al., 2018), a popular tool for viral phylogenetic inference that implements MCMC methods to explore $p(\mathbf{S}, \phi, \mathcal{G})$ and $p(\mathbf{z} | \sigma^2, \mathcal{G})$ (Cybis et al., 2015) under a range of evolutionary models. In writing this paper, we have contributed to the open-source, stand-alone library HPHAWKES <http://github.com/suchard-group/hawkes> for computing the spatiotemporal Hawkes process log-likelihood (Equation 1), its gradient (Equation 4) and its Hessian (Equation 5). HPHAWKES integrates into BEAST with the help of an application programming interface (API). Within HPHAWKES, we combine C++ code with which standard compilers generate vectorized CPU-specific instructions and OPENCL kernels that allow for GPU-specific optimization. Finally, we have used the RCPP package (Eddelbuettel and François, 2011) to make the same massive parallelization speedups available to users of the R programming language.

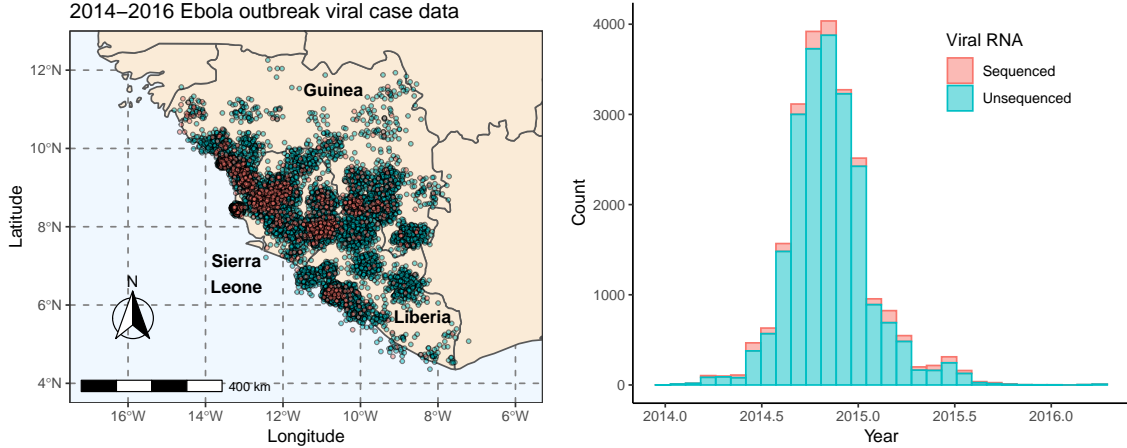


Figure 3: Spatiotemporal distribution of 23,178 viral cases during the 2014-2016 Ebola outbreak in Guinea, Sierra Leone and Liberia. Of this number, 1,367 viral samples yield RNA sequence data and interface directly with the prior over phylogenetic trees. All cases, both sequenced and unsequenced, interface with the Hawkes process likelihood.

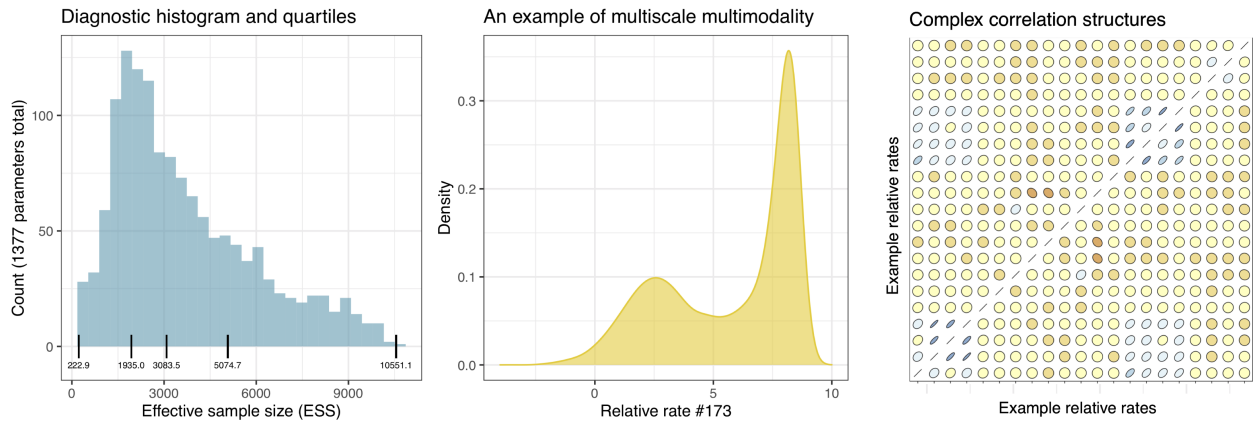


Figure 4: The posterior distribution presents multiple challenges: it is high-dimensional; it takes on different scales for different parameters; it is multimodal in some parameters; and it exhibits complex correlation structures between parameters. [Left] Histogram and quartiles from 100 million MCMC samples for the ESS of all 1377 model parameters. [Middle] Multimodal marginal posterior for a single relative rate. [Right] Posterior correlations between 21 relative rates.

3 Demonstration

3.1 Massive parallelization

Figure 2 shows benchmarking results for evaluating the Hawkes log-likelihood gradient with respect to event-specific rates θ (Equation 4). For the GPU results, we use an NVIDIA Quadro GV100, which has 5,120 CUDA cores (at 1.13 GHz) and reaches an (unboosted) 2.9 teraflops peak double-precision floating point performance (or 5.8 teraflops for fused operations such as fused multiply-add). We use a Linux machine with two 26-core Intel Xeon

| Hierarchical model module | Model parameter | Symbol | Posterior mean (95% HPD cred. int.) | Unit |
|---------------------------|--------------------------------------|-------------------------------|-------------------------------------|----------|
| Hawkes process | Background spatial lengthscale | τ_x | 194 (147, 243) | km |
| | Self-excitatory temporal lengthscale | $1/\omega$ | 29.8 (28.5, 30.9) | days |
| | Self-excitatory spatial lengthscale | h | 7.37 (7.13, 7.62) | km |
| | Normalized self-excitatory weight | $\theta_0/(\theta_0 + \mu_0)$ | 0.96 (0.95, 0.97) | — |
| | Temporal trend coefficient | β | -2.22 (-2.37,-2.06) | — |
| Phylogenetic diffusion | Standard deviation | σ | 51.0 (46.4, 55.7) | log rate |

Table 2: Posterior means and 95% highest posterior density (HPD) credible intervals from the application of the phylogenetic Hawkes process to the 2014-2016 Ebola outbreak in Guinea, Sierra Leone and Liberia.

Gold processors (2.1 GHz) for CPU results. Each physical core supports 2 threads or logical cores, and the machine achieves a peak performance of 874 gigaflops with double-precision floating point enhanced with AVX vectorization (again, double this for fused operations). Based on peak double-precision floating point operations, our *a priori* expectation is for fully parallelized GPU-based gradient evaluations to be roughly 3.3 times faster than 104-threaded AVX evaluations on the CPU.

On the left of Figure 2, we compare relative efficiency for GPU and various CPU implementations of the log-likelihood gradient and Hessian for 25,000 simulated data points using single-threaded AVX computing (15.7 and 16.3 seconds per gradient and Hessian evaluations) as baseline. Using SSE or non-vectorized single-threaded computing results in 1.5- and 2.2-fold slowdowns for the gradient and 1.3- and 2.1-fold slowdowns for the Hessian. Sticking with AVX processing, we see diminishing returns as we increase the number of threads. For the both the gradient and the Hessian, the 14- 54- and 104-thread AVX implementations are roughly 13, 33 and 41 times faster than single-threaded AVX. Agreeing with our *a priori* expectations, the GPU implementation is 140.4 times faster than single-threaded AVX and 3.5 times faster than 104-threaded AVX for the gradient and 120.0 times faster than single-threaded AVX and 2.9 times faster than 104-threaded AVX for the Hessian. The right of Figure 2 demonstrates the $\mathcal{O}(N^2)$ computational complexity for the same gradient and Hessian evaluations by varying the number of data points from 10,000 to 90,000. While parallelization does not overcome this quadratic scaling, it does reduce computational costs for finite observation counts.

3.2 2014-2016 Ebola outbreak in West Africa

During the 2014-2016 outbreak in Guinea, Sierra Leone and Liberia, Ebola viral fever resulted in over 28,000 known cases and 11,000 known deaths (World Health Organization, 2015). First reports of the virus in Guinea emerged during March of 2014 (Baize et al., 2014). At around the same time, viral cases with the same Guinean origin (Gire et al., 2014) emerged in Sierra Leone and Liberia. In May 2014, the virus crossed from Guinea to Kailahun, Sierra Leone. From there, it spread to multiple counties of Liberia and Guinea (Dudas et al., 2017), and the same strain reached Freetown, the capital of Sierra Leone, by July 2014. In the fall of 2014, Sierra Leone and Liberia were detecting 500 and 700 new cases a week. Only by

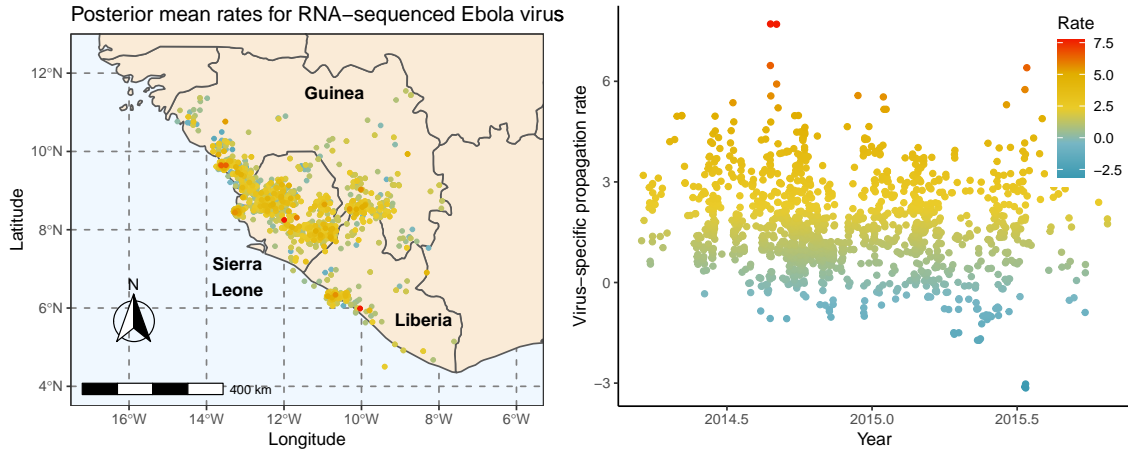


Figure 5: Hawkes model posterior mean rates θ for the 1,367 (of 1,610) RNA-sequenced viral samples for which date/location data are available. Unsurprisingly, the largest relative rates occur within or nearby major clusters of events. Adjusting for downward trends in case data with a negative coefficient β (Table 2) allows detection of higher relative rates after peak outbreak (late 2014) including a jump in infections mid-2015 (Figure 3).

the end of 2014 did case numbers begin to abate in most areas due to control measures. By March of 2015 sustained transmission of the virus only continued in western Guinea and western Sierra Leone (Dudas et al., 2017). Figure 3 shows the spatiotemporal distribution of the majority of known Ebola virus cases during the epidemic.

Using our high performance computing framework, we apply the phylogenetic Hawkes process to the analysis of 23,422 viral cases. Dudas et al. (2017) provide a total of 1,610 cases furnishing genomic sequencing, 1,367 of which come with date and location data (<https://github.com/ebov/space-time>). We supplement this sequenced data with 21,811 date and location pairs from unsequenced cases documented by the World Health Organization (<https://apps.who.int/gho/data/node.ebola-sitrep>). The precision of the spatial data is district or county level. To leverage spatial information as much as practically possible within our Hawkes model, we assume the locations follow a Gaussian distribution at district population centroids and with variance guaranteeing a 95% probability of the case occurring within the circle of equal area to the district and centered at the population centroid. We then integrate over uncertainty with respect to these locations by periodically sampling new locations according to the assumed Gaussian distribution throughout the MCMC run and with a period of roughly 100 iterations. That said, sensitivity analyses show that model inference is robust to fixing randomly generated locations for the entire MCMC chain. We make the combined data and documentation for our entire BEAST analysis available within the single file `Final.xml` and place this as well as other project scripts together at the repository <https://github.com/suchard-group/EBOVPhyloHawkes>. In addition to the software mentioned in the previous section, we make use of the `GGPLOT2` and `GGMAP` R packages for data and results visualization (Wickham, 2016; Kahle and Wickham, 2013).

For the phylogenetic prior specification $p(\mathbf{S}, \phi, \mathcal{G})$, we follow the phylogeographic analysis of Dudas et al. (2017) and use a mixture of 1,000 phylogenetic trees obtained as high-probability posterior samples from their purely phylogenetic analysis of the 1,610 sequenced

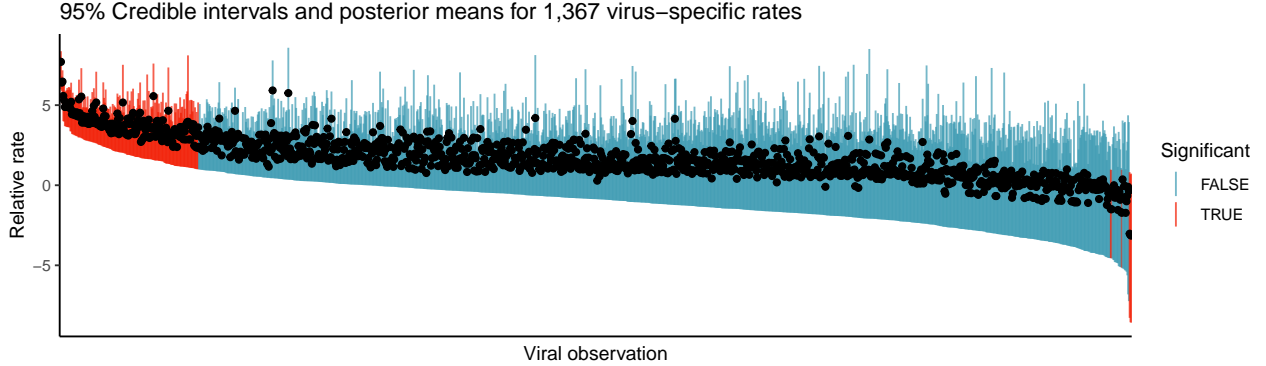


Figure 6: 95% credible intervals and posterior means for virus-specific rates θ corresponding to the subset of 1,610 sequenced viruses that come with date/location data and therefore appear in the Hawkes process module. We call those 183 intervals which do not include 1 ‘significant’. Of these, 177 are above and 6 below 1. Appendix B has labels, locations and times for each.

viral samples. In that preceding Bayesian analysis, Dudas et al. (2017) combine an HKY+ Γ_4 substitution model prior for molecular evolution (Hasegawa et al., 1985; Yang, 1994), a relaxed molecular clock prior on rates (Drummond et al., 2006a), a non-parametric coalescent ‘Skygrid’ prior on effective population size dynamics (Gill et al., 2013) and a continuous time Markov chain reference prior for overall rate (Ferreira and Suchard, 2008). We assume *a priori* that the background lengthscale τ_x follows a diffuse inverse gamma distribution with shape 1 and scale 10, where distance units are latitudinal and longitudinal degrees. An inverse gamma distribution with shape and scale parameters equal to 2 and 0.5 for both h and $1/\omega$ encodes our beliefs that self-excitatory dynamics occur at finer spatiotemporal scales, where years are the temporal units. We upweight self-excitatory dynamics by giving θ_0 and μ_0 gamma priors with shape parameters 1 and 2 and scale parameters 0.001 and 2, respectively. We absorb τ_0 into σ and place a tight inverse gamma prior on $1/\sigma$ with shape and scale parameters of 2 and 0.5. Finally, we set $\mathbf{f}(t_n) = t_n$ and place a normal prior on the univariate coefficient β with mean 0 and standard deviation of 10. We find all parameters robust to prior specification due to the large number of observations considered.

We generate 100 million MCMC samples according to the routine outlined in Section 2.3 and discard the first 500 thousand as burn-in. Using our parallel computing algorithms and a single NVIDIA GV100 GPU (Section 3.1), the routine requires 6.77 hours to generate 1 million samples and 28 days to generate all 100 million samples. Figure 4 shows the distribution of effective samples sizes (ESS) across all model parameters and illustrates some of the challenges facing any MCMC routine for the phylogenetic Hawkes model. Namely, the posterior distribution is high-dimensional, multimodal, multiscale and has complex correlation structures.

Table 2 shows posterior means and 95% highest posterior density (HPD) credible intervals for the phylogenetic Hawkes process parameters. The posterior mean for the spatial bandwidth τ_x of the Hawkes background process is 194 km (147, 243), allowing the model to incorporate and adapt to large scale geographic movement. On the other hand, the Hawkes process self-excitatory spatial bandwidth h has a posterior mean of 7.4 km (7.1,

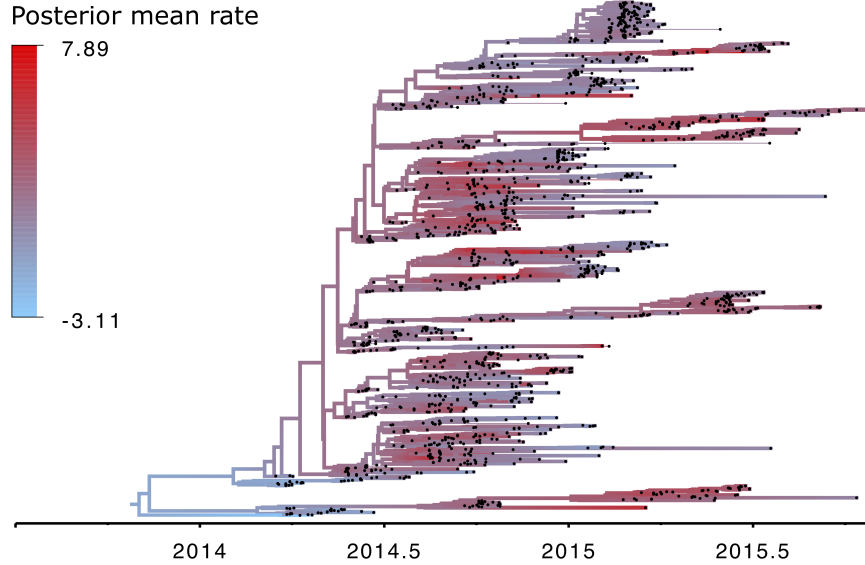


Figure 7: Posterior mean virus-specific relative rates color the posterior maximum clade credibility tree of phylogeny \mathcal{G} , a few subtrees of which potentially demonstrate elevated contagiousness.

7.6), indicating the smaller local scale for which the model attributes viral contagion. The self-excitatory temporal bandwidth $1/\omega$ has a posterior mean of 29.8 days (28.5, 30.9), indicating the timescale for which the model attributes the same viral contagion. The normalized self-excitatory weight $\theta_0/(\theta_0 + \mu_0)$ indicates the proportion of events the model attributes to self-excitatory (compared to background) dynamics and has a posterior mean of 0.96 (0.95, 0.97). The posterior mean of the self-excitatory rate’s temporal trend coefficient β is -2.22 (-2.37, -2.06) indicates that, for every additional year and *ceteris paribus*, one should expect a multiplicative decrease of $1 - \exp(-2.22) \times 100 \approx 90\%$ to the process self-excitatory rate. In this way, the model adjusts for downward trends arising from epidemiological control (e.g., mass quarantine and travel restrictions) and controls for these factors when inferring virus-specific relative rates.

Next, we consider posterior inference of the virus-specific rates θ for those viral observations that provide RNA sequences. When interpreting these results, it is important to understand that the phylogenetic Hawkes process implicitly assumes that such samples spark nearby contagion as described by spatial and temporal bandwidths h and $1/\omega$. Recall that the posteriors for these two parameters concentrate at over 7 km and 4 weeks, respectively. Figure 5 depicts the relationship between posterior mean values of θ and the spatiotemporal distribution of corresponding viruses. Since these rates represent multiplicative factors of the global self-excitatory weight θ_0 , a null value would be 1. Posterior means range from approximately -2.5 to 7.5 and increasingly vary as a function of time. As one might expect, the highest rates appear near or within larger clusters. Thanks to the negative temporal trend coefficient β and the increase of uncertainty with time, larger rate values do obtain for some viral cases occurring in 2015, despite following after peak epidemic. Figure 6 features posterior means and 95% intervals for the same virus-specific rates. Only a small subset of 183 rate intervals do not include 1. Of these, 177 have lower bound greater than 1, and 6

have upper bound below 1. We interpret all 103 of the corresponding viruses as having statistically significantly increased or decreased contagiousness. Virus-specific labels, locations and times for all 183 appear in Appendix B.

Finally, Figure 7 shows how these posterior rates organize as a function of the inferred posterior maximum clade credibility tree \mathcal{G} . Generally speaking, shorter branch lengths indicate larger effective populations of viruses, while larger branch lengths indicate smaller. For example, the structure of the bottom subtree reflects this intuition as branches are short with many splits during peak outbreak in the second half of 2014 but become mostly long in late 2014 and the remainder of 2015. According to the phylogenetic Brownian process model outlined in Section 2.2, virus-specific rate values are more highly correlated to one another when closely located to one-another on the the phylogenetic tree. It is plausible that these correlations allow the phylogenetic Hawkes model to infer higher rates for some strains that survive late into the epidemic despite dropping case counts. The model attributes some of the highest values to strains appearing in Coyah, Conakry and Kindia, Guinea, in late 2014 and early 2015. Interestingly, the model also attributes its lowest values to cases in Kono, Sierra Leone, in early 2015. Taken together, Figure 7 and the significant virus lists of Appendix B may provide helpful leads for epidemiologists searching for variants with heightened relative rates of contagion.

4 Discussion

We propose the phylogenetic Hawkes process, a Bayesian hierarchical model that relates viral spatial contagion to molecular evolution by uniting the two epidemiological paradigms of self-exciting point process and phylogenetic modeling. Due to difficulties in scaling the model to larger numbers of observations, we advance a computing strategy that combines HMC, dynamic programming and massive parallelization for key inferential bottlenecks. Finally, we apply our novel model and high performance computing framework to the analysis of over 23,000 viral cases arising from the 2014-2016 Ebola outbreak in West Africa, and Ebola strains and subtrees with plausibly higher degrees of contagiousness reveal themselves.

Unfortunately, the current model will fail when applied to the analysis of a global pandemic due to the dominant role of non-local, large scale transportation networks in propagating viral spread (Holbrook et al., 2020). We are particularly interested in developing extensions to the phylogenetic Hawkes process that leverage recent advances in scaling high-dimensional multivariate Hawkes processes (Nickel and Le, 2020) and applying the resulting multivariate phylogenetic Hawkes process to the analysis of global pandemics. In this context, each additional dimension will represent an additional country or province. Prodigious computational challenges are inevitable, and we suspect that non-trivial GPU implementations will be necessary for big data applications.

Moving beyond inference, a major question is whether the phylogenetic Hawkes process can be useful for prediction of spatial contagion and dynamics. Here, recent neural network extensions of the Hawkes process might prove useful (Mei and Eisner, 2017; Zuo et al., 2020; Zhang et al., 2020), but it is unclear what forward simulation of phylogenetic branching dynamics would look like in the context of a Hawkes process. Moreover, generating samples from the posterior predictive distribution of a Hawkes process would be extremely time

consuming when one is conditioning on millions of posterior samples. To work around this, one could perhaps parallelize over fixed parameter settings the algorithm of [Dassios and Zhao \(2011\)](#) for simulating Hawkes processes when the temporal triggering function is exponential. Such an implementation would require efficient use of parallel pseudo-random number generators ([Salmon et al., 2011](#)).

Acknowledgments

The research leading to these results has received funding through National Institutes of Health grants K25 AI153816, U19 AI135995 and R01 AI153044 and National Science Foundation grant DMS1264153. We gratefully acknowledge support from NVIDIA Corporation and Advanced Micro Devices, Inc. with the donation of parallel computing resources used for this research.

A The likelihood integral with event-specific rates

Without loss of generality, we consider the temporal Hawkes process with constant background rate. To compute the likelihood (Equation 1), we must calculate the integral

$$\begin{aligned}
\Lambda(t_N) &= \int_0^{t_N} \lambda(t) dt = \int_0^{t_N} \left(\mu + \theta_0 \sum_{t_n < t} \theta_n \omega e^{-\omega(t-t_n)} \right) dt \\
&= \int_0^{t_1} \mu dt + \sum_{n=1}^{N-1} \int_{t_n}^{t_{n+1}} \left(\mu + \theta_0 \sum_{t_n < t} \theta_n \omega e^{-\omega(t-t_n)} \right) dt \\
&= \mu t_N + \theta_0 \omega \sum_{n=1}^{N-1} \int_{t_n}^{t_{n+1}} \sum_{n'=1}^n \theta_{n'} e^{-\omega(t-t_{n'})} dt \\
&= \mu t_N + \theta_0 \omega \sum_{n=1}^{N-1} \sum_{n'=1}^n \theta_{n'} \int_{t_n}^{t_{n+1}} e^{-\omega(t-t_{n'})} dt \\
&= \mu t_N - \theta_0 \sum_{n=1}^{N-1} \sum_{n'=1}^n \theta_{n'} \left(e^{-\omega(t_{n+1}-t_{n'})} - e^{-\omega(t_n-t_{n'})} \right),
\end{aligned}$$

and we further simplify the double summation in the following.

Claim 1. *The temporal Hawkes process with rate function*

$$\lambda(t) = \mu + \theta_0 \sum_{t_n < t} \theta_n \omega e^{-\omega(t-t_n)} \tag{6}$$

admits the integral

$$\Lambda(t_N) = \int_0^{t_N} \lambda(t) dt = \mu t_N - \theta_0 \sum_{n=1}^{N-1} \theta_n \left(e^{-\omega(t_N-t_n)} - 1 \right). \tag{7}$$

Proof. Proceeding by induction, the assertion is trivial for $N = 1$. If it is true for some $N > 0$, this implies that

$$\sum_{n=1}^{N-1} \sum_{n'=1}^n \theta_{n'} (e^{-\omega(t_{n+1}-t_{n'})} - e^{-\omega(t_n-t_{n'})}) = \sum_{n=1}^{N-1} \theta_n (e^{-\omega(t_N-t_n)} - 1) .$$

It follows that

$$\begin{aligned} \Lambda(t_{N+1}) &= \mu t_{N+1} - \theta_0 \sum_{n=1}^N \sum_{n'=1}^n \theta_{n'} (e^{-\omega(t_{n+1}-t_{n'})} - e^{-\omega(t_n-t_{n'})}) \\ &= \mu (t_{N+1} - t_N) - \theta_0 \sum_{n'=1}^N \theta_{n'} (e^{-\omega(t_{N+1}-t_{n'})} - e^{-\omega(t_N-t_{n'})}) \\ &\quad + \mu t_N - \theta_0 \sum_{n=1}^{N-1} \sum_{n'=1}^n \theta_{n'} (e^{-\omega(t_{n+1}-t_{n'})} - e^{-\omega(t_n-t_{n'})}) \\ &= \mu (t_{N+1} - t_N) - \theta_0 \sum_{n'=1}^N \theta_{n'} (e^{-\omega(t_{N+1}-t_{n'})} - e^{-\omega(t_N-t_{n'})}) + \Lambda(t_N) \\ &= \mu (t_{N+1} - t_N) - \theta_0 \sum_{n'=1}^N \theta_{n'} (e^{-\omega(t_{N+1}-t_{n'})} - e^{-\omega(t_N-t_{n'})}) \\ &\quad + \mu t_N - \theta_0 \sum_{n=1}^{N-1} \theta_n (e^{-\omega(t_N-t_n)} - 1) \\ &= \mu t_{N+1} - \theta_0 \sum_{n=1}^N \theta_n (e^{-\omega(t_{N+1}-t_n)} - e^{-\omega(t_N-t_n)}) \\ &\quad - \theta_0 \sum_{n=1}^{N-1} \theta_n (e^{-\omega(t_N-t_n)} - 1) \\ &= \mu t_{N+1} - \theta_0 \sum_{n=1}^N \theta_n (e^{-\omega(t_{N+1}-t_n)} - 1) , \end{aligned}$$

thus completing the proof. □

B Viruses with statistically significant relative rates

The following observed viruses have relative rates for which the 95% credible intervals have lower bound greater than 1.

| | | | |
|---|--|----|--|
| 1 | EBOV EM_COY_2015_013857 GIN Forecariah 2015-03-18 | 8 | EBOV EM_COY_2015_016743 GIN Boke 2015-05-19 |
| 2 | EBOV EM_COY_2015_013731 GIN Coyah 2015-03-14 | 9 | EBOV KG88 GIN Boke 2015-06-19 |
| 3 | EBOV EM_COY_2015_014261 GIN Forecariah 2015-04-02 | 10 | EBOV KG90 GIN Boke 2015-06-19 |
| 4 | EBOV IPDPFHGINSP_GUI_2015_5339 GIN Conakry 2015-04-08 | 11 | EBOV KG87 GIN Boke 2015-06-19 |
| 5 | EBOV KG12 GIN Boke 2015-05-27 | 12 | EBOV KG80 GIN Boke 2015-06-18 |
| 6 | EBOV EM_COY_2015_017091 GIN Boke 2015-05-28 | 13 | EBOV KG35 GIN Boke 2015-06-08 |
| 7 | EBOV EM_COY_2015_016483 GIN Boke 2015-05-13 | 14 | EBOV GUI_CTS_2015_0052 GIN Boke 2015-06-25 |

| | | | |
|----|---|-----|---|
| 15 | EBOV GUI_CTS_2015_0050 GIN Boke 2015-06-20 | 97 | EBOV 13031_EMLH KU296665 SLE WesternUrban 2015-05-18 |
| 16 | EBOV GUI_CTS_2015_0051 GIN Boke 2015-06-21 | 98 | EBOV DML13828 SLE WesternUrban 2015-06-22 |
| 17 | EBOV KG91 GIN Boke 2015-06-20 | 99 | EBOV 20143716 KR653292 SLE Moyamba 2014-11-04 |
| 18 | EBOV KG45 GIN Boke 2015-06-09 | 100 | EBOV 20144610 KR653270 SLE Tonkolili 2014-11-12 |
| 19 | EBOV EM_C0Y_2015_017574 GIN Boke 2015-06-10 | 101 | EBOV J0021 KP759756 SLE Bombali 2014-09-29 |
| 20 | EBOV IPDPFHGINSP_GUI_2015_6899 GIN Boke 2015-05-14 | 102 | EBOV PL5260 KU296591 SLE Kambia 2015-03-23 |
| 21 | EBOV EM_C0Y_2015_014102 GIN Conakry 2015-03-26 | 103 | EBOV EM_C0Y_2015_013962 GIN Forecariah 2015-03-22 |
| 22 | EBOV IPDPFHGINSP_GUI_2015_4909 GIN Conakry 2015-03-29 | 104 | EBOV EM_C0Y_2015_013671 GIN Coyah 2015-03-12 |
| 23 | EBOV IPDPFHGINSP_GUI_2015_5117 GIN Dubreka 2015-04-03 | 105 | EBOV PL4347 KU296720 SLE Kambia 2015-03-04 |
| 24 | EBOV IPDPFHGINSP_GUI_2015_4786 GIN Conakry 2015-03-26 | 106 | EBOV EM_C0Y_2015_015815 GIN Fria 2015-04-14 |
| 25 | EBOV EM_C0Y_2015_014098 GIN Conakry 2015-03-26 | 107 | EBOV IPDPFHGINSP_GUI_2015_5038 GIN Conakry 2015-04-01 |
| 26 | EBOV EM_C0Y_2015_014100 GIN Conakry 2015-03-26 | 108 | EBOV EM_C0Y_2015_016414 GIN Dubreka 2015-05-11 |
| 27 | EBOV 1648 KR534569 GIN Kindia 2014-10-23 | 109 | EBOV EM_C0Y_2015_017865 GIN Dubreka 2015-06-18 |
| 28 | EBOV 20140174 KR653294 SLE WesternUrban 2014-08-27 | 110 | EBOV REDC-GUI-2015-00502 GIN Conakry 2015-07-13 |
| 29 | EBOV 20144521 KR653271 SLE Kono 2014-11-12 | 111 | EBOV REDC_GUI_2015_00483 GIN Conakry 2015-07-12 |
| 30 | EBOV DML24511 KT357828 SLE Kono 2015-01-14 | 112 | EBOV REDC-GUI-2015-00402 GIN Conakry 2015-07-08 |
| 31 | EBOV 20146001 KR653237 SLE Kono 2014-11-24 | 113 | EBOV EM_C0Y_2015_017057 GIN Dubreka 2015-05-27 |
| 32 | EBOV 20141352 KR653284 SLE Kambia 2014-09-26 | 114 | EBOV EM_C0Y_2015_017135 GIN Dubreka 2015-05-29 |
| 33 | EBOV G6069.1 KR105344 SLE Kambia 2014-09-25 | 115 | EBOV EM_C0Y_2015_016800 GIN Dubreka 2015-05-20 |
| 34 | EBOV 20141997 KR653293 SLE Kono 2014-10-10 | 116 | EBOV EM_C0Y_2015_016617 GIN Dubreka 2015-05-16 |
| 35 | EBOV J0008 KP759718 SLE WesternUrban 2014-09-29 | 117 | EBOV EM_C0Y_2015_016531 GIN Dubreka 2015-05-14 |
| 36 | EBOV KT2449 KU296465 SLE WesternUrban 2014-12-05 | 118 | EBOV PL4094 KU296476 SLE Kambia 2015-02-27 |
| 37 | EBOV 20143458 KR653245 SLE Tonkolili 2014-11-01 | 119 | EBOV 14795_EMLK KU296737 SLE Kambia 2015-04-25 |
| 38 | EBOV J0016 KP759742 SLE WesternRural 2014-09-30 | 120 | EBOV EM_C0Y_2015_014370 GIN Forecariah 2015-04-07 |
| 39 | EBOV G6104.1 KR105349 SLE Moyamba 2014-09-28 | 121 | EBOV EM_C0Y_2015_013795 GIN Forecariah 2015-03-16 |
| 40 | EBOV 20141397 KR653288 SLE Moyamba 2014-09-28 | 122 | EBOV LIBR10106 KT725337 LBR Nimbal 2014-08-20 |
| 41 | EBOV G6103.1 KR105348 SLE Moyamba 2014-09-28 | 123 | EBOV LIBR10081 KT725339 LBR Margibi 2014-08-26 |
| 42 | EBOV PL6656 KU296523 SLE PortLoko 2015-05-01 | 124 | EBOV LIBR10017 KT725293 LBR Montserrado 2014-08-19 |
| 43 | EBOV PL7429 KU296617 SLE PortLoko 2015-05-29 | 125 | EBOV LIBR10170 KT725350 LBR Montserrado 2014-08-17 |
| 44 | EBOV PL7451 KU296837 SLE PortLoko 2015-05-29 | 126 | EBOV CDC-NIH-257 LBR Montserrado 2014-08-27 |
| 45 | EBOV PL7375 KU296498 SLE PortLoko 2015-05-27 | 127 | EBOV LIBR10082 KT725300 LBR Margibi 2014-08-26 |
| 46 | EBOV PL7401 KU296819 SLE PortLoko 2015-05-27 | 128 | EBOV LIBR10029 KT725348 LBR Margibi 2014-08-16 |
| 47 | EBOV G4725.1 KR105267 SLE Moyamba 2014-08-04 | 129 | EBOV LIBR10030 KT725257 LBR Margibi 2014-08-16 |
| 48 | EBOV J0038 KP759618 SLE PortLoko 2014-09-30 | 130 | EBOV LIBR10025 KT725315 LBR Margibi 2014-08-16 |
| 49 | EBOV J0102 KP759657 SLE PortLoko 2014-10-27 | 131 | EBOV LIBR10088 KT725349 LBR Montserrado 2014-08-26 |
| 50 | EBOV J0103 KP759658 SLE PortLoko 2014-10-29 | 132 | EBOV LIBR10087 KT725346 LBR Margibi 2014-08-26 |
| 51 | EBOV J0104 KP759765 SLE PortLoko 2014-10-29 | 133 | EBOV LIBR10086 KT725381 LBR Margibi 2014-08-26 |
| 52 | EBOV J0105 KP759766 SLE PortLoko 2014-10-29 | 134 | EBOV EM_075368 KR817131 GIN Macenta 2014-08-29 |
| 53 | EBOV 20141282 KR653229 SLE Kambia 2014-09-23 | 135 | EBOV EM_000015 KR817067 GIN Macenta 2014-09-01 |
| 54 | EBOV J0027 KP759678 SLE Bombali 2014-10-02 | 136 | EBOV EM_000321 KR817074 GIN Macenta 2014-09-09 |
| 55 | EBOV G6091.1 KR105346 SLE Tonkolili 2014-09-27 | 137 | EBOV EM_074785 KR817126 GIN Macenta 2014-08-16 |
| 56 | EBOV J0162 KP759622 SLE Kambia 2014-11-09 | 138 | EBOV EM_000218 KR817072 GIN Macenta 2014-09-07 |
| 57 | EBOV J0034 KP759608 SLE PortLoko 2014-09-30 | 139 | EBOV EM_000127 KR817070 GIN Gueckedou 2014-09-04 |
| 58 | EBOV 20141429 KR653260 SLE Kono 2014-09-28 | 140 | EBOV EM_000028 KR817069 GIN Macenta 2014-09-01 |
| 59 | EBOV G6089.1 KR105345 SLE Tonkolili 2014-09-27 | 141 | EBOV EM_000502 KR817078 GIN Macenta 2014-09-13 |
| 60 | EBOV G6095.1 KR105347 SLE Tonkolili 2014-09-27 | 142 | EBOV EM_001102 KR817089 GIN Lola 2014-10-05 |
| 61 | EBOV 20142551 KR653226 SLE Koinadugu 2014-10-23 | 143 | EBOV Conakry_645 KR534513 GIN Macenta 2014-08-14 |
| 62 | EBOV 20143648 KR653253 SLE Koinadugu 2014-11-03 | 144 | EBOV EM_074548 KR817123 LBR Lofa 2014-08-08 |
| 63 | EBOV 20143938 KR653264 SLE Koinadugu 2014-11-07 | 145 | EBOV EM_078416 KR817161 GIN Faranah 2014-11-24 |
| 64 | EBOV 20143659 KR653256 SLE Koinadugu 2014-11-03 | 146 | EBOV EM_078415 KR817160 GIN Faranah 2014-11-24 |
| 65 | EBOV 20142895 KR653268 SLE Koinadugu 2014-10-24 | 147 | EBOV EM_075447 KR817134 GIN Macenta 2014-08-31 |
| 66 | EBOV 20141271 KR653261 SLE PortLoko 2014-09-24 | 148 | EBOV EM_075373 KR817132 GIN Macenta 2014-08-30 |
| 67 | EBOV J0084 KP759753 SLE PortLoko 2014-10-16 | 149 | EBOV 789 KR534523 GIN Dubreka 2014-08-29 |
| 68 | EBOV J0083 KP759752 SLE PortLoko 2014-10-18 | 150 | EBOV 1622 KR534567 GIN Nzerekore 2014-10-22 |
| 69 | EBOV J0035 KP759609 SLE PortLoko 2014-10-01 | 151 | EBOV EM_075435 KR817133 GIN Kerouane 2014-08-30 |
| 70 | EBOV J0058 KP759724 SLE PortLoko 2014-10-08 | 152 | EBOV EM_004201 KR817093 GIN Kissidougou 2014-12-24 |
| 71 | EBOV J0071 KP759736 SLE PortLoko 2014-10-09 | 153 | EBOV EM_004259 KR817094 GIN Kissidougou 2014-12-26 |
| 72 | EBOV 20140024 KR653252 SLE PortLoko 2014-08-20 | 154 | EBOV EM_004290 KR817095 GIN Kissidougou 2014-12-27 |
| 73 | EBOV G4972.1 KR105285 SLE Kenema 2014-08-14 | 155 | EBOV EM_078722 KR817175 GIN Kissidougou 2014-12-16 |
| 74 | EBOV 20140433 KR653246 SLE Tonkolili 2014-09-03 | 156 | EBOV EM_078779 KR817177 GIN Kissidougou 2014-12-18 |
| 75 | EBOV J0030 KP759606 SLE PortLoko 2014-10-03 | 157 | EBOV EM_078694 KR817171 GIN Kissidougou 2014-12-14 |
| 76 | EBOV J0011 KP759641 SLE PortLoko 2014-09-29 | 158 | EBOV EM_004059 KR817090 GIN Kissidougou 2014-12-20 |
| 77 | EBOV 20141288 KR653232 SLE PortLoko 2014-09-23 | 159 | EBOV EM_078706 KR817173 GIN Kissidougou 2014-12-15 |
| 78 | EBOV J0013 KP759643 SLE PortLoko 2014-09-28 | 160 | EBOV EM_004085 KR817091 GIN Kissidougou 2014-12-19 |
| 79 | EBOV J0014 KP759740 SLE PortLoko 2014-09-29 | 161 | EBOV EM_078763 KR817176 GIN Kissidougou 2014-12-17 |
| 80 | EBOV J0114 KP759596 SLE PortLoko 2014-10-29 | 162 | EBOV LIBR0284 KT725328 LBR GrandCapeMount 2014-11-22 |
| 81 | EBOV J0115 KP759597 SLE PortLoko 2014-10-29 | 163 | EBOV CDC-NIH-3832 LBR GrandCapeMount 2014-11-23 |
| 82 | EBOV G4956.1 KR105282 SLE Tonkolili 2014-08-13 | 164 | EBOV LIBR0286 KR006952 LBR GrandCapeMount 2014-11-22 |
| 83 | EBOV 20140134 KR653227 SLE Bombali 2014-08-26 | 165 | EBOV LIBR10103 KT725338 LBR Nimbal 2014-08-20 |
| 84 | EBOV J0020 KP759755 SLE Bombali 2014-09-25 | 166 | EBOV LIBR10035 KT725259 LBR GrandBassa 2014-08-15 |
| 85 | EBOV J0019 KP759754 SLE Bombali 2014-09-25 | 167 | EBOV EM_074438 KR817118 GIN Nzerekore 2014-08-01 |
| 86 | EBOV J0022 KP759757 SLE Bombali 2014-09-25 | 168 | EBOV EM_000706 KR817079 GIN Nzerekore 2014-09-21 |
| 87 | EBOV J0017 KP759747 SLE Bombali 2014-09-26 | 169 | EBOV EM_074439 KR817119 GIN Nzerekore 2014-08-01 |
| 88 | EBOV 20142260 KR653262 SLE Bombali 2014-10-14 | 170 | EBOV EM_074436 KR817116 GIN Nzerekore 2014-08-01 |
| 89 | EBOV J0096 KP759654 SLE WesternUrban 2014-10-27 | 171 | EBOV EM_074437 KR817117 GIN Nzerekore 2014-08-01 |
| 90 | EBOV J0015 KP759741 SLE Bombali 2014-09-26 | 172 | EBOV LIBR10127 KT725272 LBR Bong 2014-08-22 |
| 91 | EBOV 20141232 KR653266 SLE Tonkolili 2014-09-25 | 173 | EBOV LIBR0071 KT725303 LBR GrandBassa 2014-11-06 |
| 92 | EBOV 20142127 KR653234 SLE Bombali 2014-10-12 | 174 | EBOV LIBR0059 KR006941 LBR RiverCess 2014-11-05 |
| 93 | EBOV 20141497 KR653273 SLE Bombali 2014-10-01 | 175 | EBOV LIBR0058 KR006940 LBR RiverCess 2014-11-05 |
| 94 | EBOV G5743.1 KR105323 SLE Kono 2014-09-17 | 176 | EBOV EMO95 KM034550 SLE Kailahun 2014-05-25 |
| 95 | EBOV G5529.1 KR105309 SLE Kono 2014-09-05 | 177 | EBOV G3676 KM034554 SLE Kailahun 2014-05-27 |
| 96 | EBOV 12854_EMLH KU296729 SLE WesternUrban 2015-04-15 | | |

The following observed viruses have relative rates for which the 95% credible intervals have upper bound less than 1.

- 1 EBOV|EM_079413|KR817184|GIN|Gueckedou|2014-03-31
- 2 EBOV|EM_079414|KR817185|GIN|Gueckedou|2014-03-31
- 3 EBOV|EM_079542|KR817199|GIN|Gueckedou|2014-04-12

C Parallelized gradient algorithms

Algorithms 1 and 2 present instructions for computing the Hawkes process log-likelihood gradient (Equation 4) with respect to the M -vector θ of event-specific rates. Figure 2 shows resulting speedups for both Algorithm (1) and Algorithm (2) on a CPU and GPU, respectively.

References

- Bacry, E., I. Mastromatteo, and J.-F. Muzy. 2015. Hawkes processes in finance. *Market Microstructure and Liquidity* 1:1550005.
- Baize, S., D. Pannetier, L. Oestereich, T. Rieger, L. Koivogui, N. Magassouba, B. Soropogui, M. S. Sow, S. Keïta, H. De Clerck, et al. 2014. Emergence of zaire ebola virus disease in guinea. *New England Journal of Medicine* 371:1418–1425.
- Bertozzi, A. L., E. Franco, G. Mohler, M. B. Short, and D. Sledge. 2020. The challenges of modeling and forecasting the spread of covid-19. *Proceedings of the National Academy of Sciences* 117:16732–16738.
- Boni, M. F., P. Lemey, X. Jiang, T. T.-Y. Lam, B. W. Perry, T. A. Castoe, A. Rambaut, and D. L. Robertson. 2020. Evolutionary origins of the sars-cov-2 sarbecovirus lineage responsible for the covid-19 pandemic. *Nature Microbiology* 5:1408–1417.
- Brockmann, D. and D. Helbing. 2013. The hidden geometry of complex, network-driven contagion phenomena. *science* 342:1337–1342.
- Cavalli-Sforza, L. L. and A. W. Edwards. 1967. Phylogenetic analysis. models and estimation procedures. *American Journal of Human Genetics* 19:233–257.
- Chiang, W.-H., X. Liu, and G. Mohler. 2020. Hawkes process modeling of covid-19 with mobility leading indicators and spatial covariates. *medRxiv* .
- Cybis, G., J. Sinsheimer, T. Bedford, A. Mather, P. Lemey, and M. Suchard. 2015. Assessing phenotypic correlation through the multivariate phylogenetic latent liability model. *Annals of Applied Statistics* 9:969 – 991.
- Daley, D. J. and D. V. Jones. 2003. *An Introduction to the Theory of Point Processes: Elementary Theory of Point Processes*. Springer.
- Dassios, A. and H. Zhao. 2011. A dynamic contagion process. *Advances in applied probability* 43:814–846.

- Drummond, A., S. Ho, M. Phillips, and A. Rambaut. 2006a. Relaxed phylogenetics and dating with confidence. *PLoS Biology* 4:e88.
- Drummond, A. J., S. Y. Ho, M. J. Phillips, and A. Rambaut. 2006b. Relaxed phylogenetics and dating with confidence. *PLoS Biol* 4:e88.
- Dudas, G., L. M. Carvalho, T. Bedford, A. J. Tatem, G. Baele, N. R. Faria, D. J. Park, J. T. Ladner, A. Arias, D. Asogun, et al. 2017. Virus genomes reveal factors that spread and sustained the ebola epidemic. *Nature* 544:309–315.
- Eddelbuettel, D. and R. François. 2011. Rcpp: Seamless R and C++ integration. *Journal of Statistical Software* 40:1–18.
- Faria, N. R., A. Rambaut, M. A. Suchard, G. Baele, T. Bedford, M. J. Ward, A. J. Tatem, J. D. Sousa, N. Arinaminpathy, J. Pépin, et al. 2014. The early spread and epidemic ignition of hiv-1 in human populations. *science* 346:56–61.
- Felsenstein, J. 1978. The number of evolutionary trees. *Systematic zoology* 27:27–33.
- Felsenstein, J. 1985. Phylogenies and the comparative method. *American Naturalist* 125:1–15.
- Ferreira, M. A. and M. A. Suchard. 2008. Bayesian analysis of elapsed times in continuous-time markov chains. *Canadian Journal of Statistics* 36:355–368.
- Fisher, A. A., X. Ji, Z. Zhang, P. Lemey, and M. A. Suchard. 2021. Relaxed random walks at scale. *Systematic Biology* .
- Fox, E. W., F. P. Schoenberg, J. S. Gordon, et al. 2016. Spatially inhomogeneous background rate estimators and uncertainty quantification for nonparametric hawkes point process models of earthquake occurrences. *The Annals of Applied Statistics* 10:1725–1756.
- Freckleton, R. P. 2012. Fast likelihood calculations for comparative analyses. *Methods in Ecology and Evolution* 3:940–947.
- Gill, M. S., P. Lemey, N. R. Faria, A. Rambaut, B. Shapiro, and M. A. Suchard. 2013. Improving bayesian population dynamics inference: a coalescent-based model for multiple loci. *Molecular biology and evolution* 30:713–724.
- Gire, S. K., A. Goba, K. G. Andersen, R. S. Sealfon, D. J. Park, L. Kanneh, S. Jalloh, M. Momoh, M. Fullah, G. Dudas, et al. 2014. Genomic surveillance elucidates ebola virus origin and transmission during the 2014 outbreak. *science* 345:1369–1372.
- Haario, H., E. Saksman, J. Tamminen, et al. 2001. An adaptive metropolis algorithm. *Bernoulli* 7:223–242.
- Habbema, J., H. JDF, K. Van den Broek, et al. 1974. A stepwise discriminant analysis program using density estimation. .

- Hasegawa, M., H. Kishino, and T.-a. Yano. 1985. Dating of the human-ape splitting by a molecular clock of mitochondrial dna. *Journal of molecular evolution* 22:160–174.
- Hawkes, A. 1972. Spectra of some mutually exciting point processes with associated variables. *Stochastic point processes* Pages 261–271.
- Hawkes, A. 1973. Cluster models for earthquakes-regional comparisons. *Bull. Int. Stat. Inst.* 45:454–461.
- Hawkes, A. G. 1971a. Point spectra of some mutually exciting point processes. *Journal of the Royal Statistical Society: Series B (Methodological)* 33:438–443.
- Hawkes, A. G. 1971b. Spectra of some self-exciting and mutually exciting point processes. *Biometrika* 58:83–90.
- Hawkes, A. G. 2018. Hawkes processes and their applications to finance: a review. *Quantitative Finance* 18:193–198.
- Ho, L. S. T. and C. Ané. 2014. A linear-time algorithm for Gaussian and non-Gaussian trait evolution models. *Systematic Biology* 3:397–402.
- Holbrook, A. J., P. Lemey, G. Baele, S. Dellicour, D. Brockmann, A. Rambaut, and M. A. Suchard. 2020. Massive parallelization boosts big bayesian multidimensional scaling. *Journal of Computational and Graphical Statistics* Pages 1–34.
- Holbrook, A. J., C. E. Loeffler, S. R. Flaxman, and M. A. Suchard. 2021. Scalable bayesian inference for self-excitatory stochastic processes applied to big american gunfire data. *Statistics and Computing* 31:1–15.
- Kahle, D. and H. Wickham. 2013. ggmap: Spatial visualization with ggplot2. *The R journal* 5:144–161.
- Kelly, J. D., J. Park, R. J. Harrigan, N. A. Hoff, S. D. Lee, R. Wannier, B. Selo, M. Mossoko, B. Njolo, E. Okitolonda-Wemakoy, et al. 2019. Real-time predictions of the 2018–2019 ebola virus disease outbreak in the democratic republic of the congo using hawkes point process models. *Epidemics* 28:100354.
- Kim, H. 2011. Spatio-temporal point process models for the spread of avian influenza virus (H5N1). Ph.D. thesis UC Berkeley.
- Kobayashi, R. and R. Lambiotte. 2016. Tideh: Time-dependent hawkes process for predicting retweet dynamics. *in* *Proceedings of the International AAAI Conference on Web and Social Media* vol. 10.
- Leimkuhler, B. and S. Reich. 2004. *Simulating Hamiltonian dynamics* vol. 14. Cambridge university press.
- Lemey, P., A. Rambaut, A. Drummond, and M. Suchard. 2009. Bayesian phylogeography finds its roots. *PLoS Computational Biology* 5:e1000520.

- Lemey, P., A. Rambaut, J. Welch, and M. Suchard. 2010. Phylogeography takes a relaxed random walk in continuous space and time. *Molecular Biology and Evolution* 27:1877–1885.
- Loeffler, C. and S. Flaxman. 2018. Is gun violence contagious? a spatiotemporal test. *Journal of quantitative criminology* 34:999–1017.
- Mau, B., M. A. Newton, and B. Larget. 1999. Bayesian phylogenetic inference via markov chain monte carlo methods. *Biometrics* 55:1–12.
- Mei, H. and J. M. Eisner. 2017. The neural Hawkes process: A neurally self-modulating multivariate point process. Pages 6754–6764 *in* *Advances in Neural Information Processing Systems*.
- Meyer, S., L. Held, et al. 2014. Power-law models for infectious disease spread. *The Annals of Applied Statistics* 8:1612–1639.
- Mohler, G. 2014. Marked point process hotspot maps for homicide and gun crime prediction in chicago. *International Journal of Forecasting* 30:491–497.
- Mohler, G. et al. 2013. Modeling and estimation of multi-source clustering in crime and security data. *The Annals of Applied Statistics* 7:1525–1539.
- Neal, R. M. 2011. MCMC using Hamiltonian dynamics. *Handbook of Markov Chain Monte Carlo* 2.
- Nickel, M. and M. Le. 2020. Learning multivariate hawkes processes at scale. arXiv preprint arXiv:2002.12501 .
- Ogata, Y. 1988. Statistical models for earthquake occurrences and residual analysis for point processes. *Journal of the American Statistical association* 83:9–27.
- Park, J., F. P. Schoenberg, A. L. Bertozzi, and P. J. Brantingham. 2019. Investigating clustering and violence interruption in gang-related violent crime data using spatial-temporal point processes with covariates .
- Pearl, J. 1982. Reverend Bayes on inference engines: A distributed hierarchical approach. Pages 133–136 *in* *AAAI-82: Proceedings of the Second National Conference on Artificial Intelligence*.
- Pybus, O. G., M. A. Suchard, P. Lemey, F. J. Bernardin, A. Rambaut, F. W. Crawford, R. R. Gray, N. Arinaminpathy, S. L. Stramer, M. P. Busch, et al. 2012. Unifying the spatial epidemiology and molecular evolution of emerging epidemics. *Proceedings of the National Academy of Sciences* 109:15066–15071.
- Rambaut, A., O. G. Pybus, M. I. Nelson, C. Viboud, J. K. Taubenberger, and E. C. Holmes. 2008. The genomic and epidemiological dynamics of human influenza a virus. *Nature* 453:615–619.

- Reinhart, A. 2018. A review of self-exciting spatio-temporal point processes and their applications. *Statistical Science* 33:299–318.
- Rizoiu, M.-A., Y. Lee, S. Mishra, and L. Xie. 2017. A tutorial on Hawkes processes for events in social media. *arXiv preprint arXiv:1708.06401* .
- Rizoiu, M.-A., S. Mishra, Q. Kong, M. Carman, and L. Xie. 2018. Sir-Hawkes: Linking epidemic models and Hawkes processes to model diffusions in finite populations. Pages 419–428 *in* Proceedings of the 2018 World Wide Web Conference on World Wide Web International World Wide Web Conferences Steering Committee.
- Robert, P. 1976. On the choice of smoothing parameters for parzen estimators of probability density functions. *IEEE Transactions on Computers* 25:1175–1179.
- Ronquist, F., M. Teslenko, P. Van Der Mark, D. L. Ayres, A. Darling, S. Höhna, B. Larget, L. Liu, M. A. Suchard, and J. P. Huelsenbeck. 2012. MrBayes 3.2: efficient Bayesian phylogenetic inference and model choice across a large model space. *Systematic biology* 61:539–542.
- Salmon, J. K., M. A. Moraes, R. O. Dror, and D. E. Shaw. 2011. Parallel random numbers: as easy as 1, 2, 3. Pages 1–12 *in* Proceedings of 2011 International Conference for High Performance Computing, Networking, Storage and Analysis.
- Schoenberg, F. P. 2004. Testing separability in spatial-temporal marked point processes. *Biometrics* Pages 471–481.
- Schoenberg, F. P. 2013. Facilitated estimation of η s. *Bulletin of the Seismological Society of America* 103:601–605.
- Schoenberg, F. P. 2020. Nonparametric estimation of variable productivity Hawkes processes. *arXiv preprint arXiv:2003.08858* .
- Schoenberg, F. P., M. Hoffmann, and R. J. Harrigan. 2019. A recursive point process model for infectious diseases. *Annals of the Institute of Statistical Mathematics* 71:1271–1287.
- Sinsheimer, J. S., J. A. Lake, and R. J. Little. 1996. Bayesian hypothesis testing of four-taxon topologies using molecular sequence data. *Biometrics* Pages 193–210.
- Smith, G. J., D. Vijaykrishna, J. Bahl, S. J. Lycett, M. Worobey, O. G. Pybus, S. K. Ma, C. L. Cheung, J. Raghwani, S. Bhatt, et al. 2009. Origins and evolutionary genomics of the 2009 swine-origin H1N1 influenza A epidemic. *Nature* 459:1122–1125.
- Suchard, M., C. Kitchen, J. Sinsheimer, and R. Weiss. 2003. Hierarchical phylogenetic models for analyzing multipartite sequence data. *Systematic Biology* 52:649–664.
- Suchard, M. and A. Rambaut. 2009. Many-core algorithms for statistical phylogenetics. *Bioinformatics* 25:1370–1376.
- Suchard, M., R. Weiss, and J. Sinsheimer. 2001. Bayesian selection of continuous-time Markov chain evolutionary models. *Molecular Biology and Evolution* 18:1001–1013.

- Suchard, M. A., P. Lemey, G. Baele, D. L. Ayres, A. J. Drummond, and A. Rambaut. 2018. Bayesian phylogenetic and phylodynamic data integration using BEAST 1.10. *Virus Evolution* 4:vey016.
- Wadman, M. 2021. United states rushes to fill void in viral sequencing. *Science* (New York, NY) 371:657–658.
- Wickham, H. 2016. *ggplot2: Elegant Graphics for Data Analysis*. Springer-Verlag New York.
- World Health Organization. 2015. Who: Ebola situation report 30 december 2015 .
- Yang, Z. 1994. Maximum likelihood phylogenetic estimation from dna sequences with variable rates over sites: approximate methods. *Journal of Molecular evolution* 39:306–314.
- Yang, Z. and B. Rannala. 1997. Bayesian phylogenetic inference using dna sequences: a markov chain monte carlo method. *Molecular biology and evolution* 14:717–724.
- Yuan, B., F. Schoenberg, and A. Bertozzi. 2021. Fast estimation of multivariate spatiotemporal hawkes processes and network reconstruction. *Annals of the Institute of Statistical Mathematics* Pages 1–26.
- Zhang, Q., A. Lipani, O. Kirnap, and E. Yilmaz. 2020. Self-attentive hawkes process. Pages 11183–11193 *in* International Conference on Machine Learning PMLR.
- Zhuang, J., Y. Ogata, and D. Vere-Jones. 2004. Analyzing earthquake clustering features by using stochastic reconstruction. *Journal of Geophysical Research: Solid Earth* 109.
- Zuo, S., H. Jiang, Z. Li, T. Zhao, and H. Zha. 2020. Transformer hawkes process. Pages 11692–11702 *in* International Conference on Machine Learning PMLR.

Algorithm 1 Parallel evaluation of Hawkes process log-likelihood gradient:

Makes use of multiple central processing unit (CPU) cores and loop vectorization to calculate Hawkes process log-likelihood gradient with respect to event-specific rates θ . When using double-precision floating point, this algorithm may use either SSE or AVX vectorization to make $J = 2$ - or 4-long jumps. We denote the number of CPU cores as B . Symbols ℓ , λ and Λ appear in Equations (1) and (4).

```

1: Compute rates  $\lambda_1, \dots, \lambda_N$ :
a:   parfor  $b \in \{1, \dots, B\}$  do
b:     if  $b \neq B$  then
c:        $Upper \leftarrow b \lfloor N/B \rfloor$ 
d:     else
e:        $Upper \leftarrow \lceil N/B \rceil$ 
f:     end if
g:     for  $n \in \{(b-1)\lfloor N/B \rfloor + 1, \dots, Upper\}$  do
h:       copy  $\mathbf{x}_n, t_n$  to cache
i:        $\lambda_n \leftarrow \mathbf{0}$  ▷ vector of length J
j:        $n' \leftarrow 1$ 
k:       while  $n' < N$  do
l:          $J \leftarrow \min(J, N - n')$ 
m:         copy  $\mathbf{x}_{n':(n'+J)}, t_{n':(n'+J)}$  to cache
n:          $\Delta_{nn'} : \Delta_{nn':(n'+J-1)} \leftarrow (\mathbf{x}_n - \mathbf{x}_{n'}) : (\mathbf{x}_n - \mathbf{x}_{n'+J-1})$  ▷ vectorized subtraction
o:         calculate  $\delta_{nn'} : \delta_{n(n'+J-1)}$  ▷ vectorized multiplication
p:         calculate  $\lambda_{nn'} : \lambda_{n(n'+J-1)}$  ▷ vectorized evaluation
q:          $\lambda_n \leftarrow \lambda_n + \lambda_{nn'} : \lambda_{n(n'+J-1)}$  ▷ vectorized addition
r:          $n' \leftarrow n' + J$ 
s:       end while
t:     end for
u:   end parfor
2: Compute  $M$  gradients  $\frac{\partial \ell}{\partial \theta_n}$ :
a:   parfor  $b \in \{1, \dots, B\}$  do
b:     if  $b \neq B$  then
c:        $Upper \leftarrow b \lfloor M/B \rfloor$ 
d:     else
e:        $Upper \leftarrow \lceil M/B \rceil$ 
f:     end if
g:     for  $n \in \{(b-1)\lfloor M/B \rfloor + 1, \dots, Upper\}$  do
h:       copy  $\mathbf{x}_n, t_n$  to cache
i:        $\frac{\partial \ell}{\partial \theta_n} \leftarrow 0$ 
j:        $n' \leftarrow 1$ 
k:       while  $n' < N$  do
l:          $J \leftarrow \min(J, N - n')$ 
m:         copy  $\mathbf{x}_{n':(n'+J)}, t_{n':(n'+J)}$  to cache
n:          $\Delta_{nn'} : \Delta_{nn':(n'+J-1)} \leftarrow (\mathbf{x}_n - \mathbf{x}_{n'}) : (\mathbf{x}_n - \mathbf{x}_{n'+J-1})$  ▷ vectorized subtraction
o:         calculate  $\delta_{nn'} : \delta_{n(n'+J-1)}$  ▷ vectorized multiplication
p:         calculate  $e^{-\omega(t_{n'} - t_n)} \phi\left(\frac{\delta_{nn'}}{h}\right) : e^{-\omega(t_{n'+J-1} - t_n)} \phi\left(\frac{\delta_{n(n'+J-1)}}{h}\right)$  ▷ vectorized evaluation
q:         for  $j \in n', \dots, n' + J - 1$  do
r:            $\frac{\partial \ell}{\partial \theta_n} \leftarrow \frac{\partial \ell}{\partial \theta_n} + \mathcal{I}_{[t_n < t_j]} \frac{1}{\lambda_j} \frac{\partial \lambda_{jn}}{\partial \theta_n}$ 
s:         end for
t:          $n' \leftarrow n' + J$ 
u:       end while
v:        $\frac{\partial \ell}{\partial \theta_n} \leftarrow \frac{\partial \ell}{\partial \theta_n} + \theta_0 (e^{-\omega(t_N - t_n)} - 1)$ 
w:     end for
x:   end parfor

```

Algorithm 2 Parallel evaluation of Hawkes process log-likelihood gradient:

Computes the log-likelihood gradient with respect to event-specific rates θ using multiple levels of parallelization on a graphics processing unit (GPU). In this paper, we specify $B = 128$ for the size of the GPU work groups. Symbols ℓ , λ and Λ appear in Equations (1) and (4).

```

1: Compute rates  $\lambda_1, \dots, \lambda_N$ :
a:   parfor  $n \in \{1, \dots, N\}$  do
b:     copy  $\mathbf{x}_n, t_n$  to local
c:   parfor  $N' \in \{1, \dots, \lfloor N/B \rfloor\}$  do
d:      $n' \leftarrow N'$ 
e:      $\lambda_{nN'} \leftarrow 0$ 
f:     while  $n' < N$  do
g:       copy  $\mathbf{x}_{n'}, t_{n'}$  to local
h:        $\Delta_{nn'} \leftarrow \mathbf{x}_n - \mathbf{x}_{n'}$ 
i:       calculate  $\delta_{nn'} = \sqrt{\sum \Delta_{nn'} \circ \Delta_{nn'}}$ 
j:        $\lambda_{nN'} \leftarrow \lambda_{nN'} + \lambda_{nn'}$ 
k:        $n' \leftarrow n' + B$ 
l:     end while
m:   end parfor
n:    $\lambda_n \leftarrow \sum_{N'} \lambda_{nN'}$ 
o: end parfor
2: Compute  $M$  gradients  $\frac{\partial \ell}{\partial \theta_n}$ :
a:   parfor  $n \in \{1, \dots, M\}$  do
b:     copy  $\mathbf{x}_n, t_n$  to local
c:   parfor  $N' \in \{1, \dots, \lfloor N/B \rfloor\}$  do
d:      $n' \leftarrow N'$ 
e:      $\left(\frac{\partial \ell}{\partial \theta_n}\right)_{N'} \leftarrow 0$ 
f:     while  $n' < N$  do
g:       copy  $\mathbf{x}_{n'}, t_{n'}$  to local
h:        $\Delta_{nn'} \leftarrow \mathbf{x}_n - \mathbf{x}_{n'}$ 
i:       calculate  $\delta_{nn'} = \sqrt{\sum \Delta_{nn'} \circ \Delta_{nn'}}$ 
j:        $\left(\frac{\partial \ell}{\partial \theta_n}\right)_{N'} \leftarrow \left(\frac{\partial \ell}{\partial \theta_n}\right)_{N'} + \mathcal{I}_{[t_n < t_{n'}]} \frac{1}{\lambda_{n'}} \frac{\partial \lambda_{n'n}}{\partial \theta_n}$ 
k:        $n' \leftarrow n' + B$ 
l:     end while
m:   end parfor
n:    $\frac{\partial \ell}{\partial \theta_n} \leftarrow \sum_{N'} \left(\frac{\partial \ell}{\partial \theta_n}\right)_{N'}$ 
o:    $\frac{\partial \ell}{\partial \theta_n} \leftarrow \frac{\partial \ell}{\partial \theta_n} + \theta_0 (e^{-\omega(t_N - t_n)} - 1)$ 
p: end parfor

```